Crystal orientation dependent oxidation modes at the buried graphene-Cu interface

Philipp Braeuninger-Weimer[1], Oliver J. Burton[1], Patrick Zeller[2], Matteo Amati[2], Luca Gregoratti[2], Robert S. Weatherup[3], Stephan Hofmann[1]

1 Department of Engineering, University of Cambridge, Cambridge CB3 0FA, UK
2 Elettra-Sincrotrone Trieste S.C.p.A., AREA Science Park, S.S. 14 km 163.5, 34149 Trieste, Italy
3 Department of Materials, University of Oxford, Parks Road, Oxford OX1 3PH, UK

Abstract

We combine spatially-resolved scanning photoelectron spectroscopy with confocal Raman and optical microscopy to reveal how the oxidation of the buried graphene-Cu interface relates to the Cu crystallographic orientation. We analyse over one hundred different graphene covered Cu (high and low index) orientations exposed to air for 2 years. Four general oxidation modes are observed, that can be mapped as regions onto the polar plot of Cu surface orientations. These modes are: 1) complete, 2) irregular, 3) inhibited and 4) enhanced wrinkle interface oxidation. We present a comprehensive characterisation of these modes, consider the underlying mechanisms, compare air and water mediated oxidation and discuss this in the context of the diverse prior literature in this area. This understanding incorporates effects from across the wide parameter space of 2D material interface engineering, relevant to key challenges in their emerging applications, ranging from scalable transfer to electronic contacts, encapsulation and corrosion protection.

Introduction

Two dimensional layered materials have been extensively studied over the last 15 years. More recently, the importance of interface effects between 2D layers and 3D materials has gained increasing prominence. Graphene-substrate interactions play a governing role in the physical, electrical and chemical characteristics of a graphene layer. Prominent examples include the graphene transfer from a catalyst,[1–5] electronic contacts,[6–8] encapsulation of graphene device channels,[9–13] diffusion barriers for Cu interconnects[14,15] and corrosion protection effects that 2D materials can provide for 3D materials.[16,17] Depending on the device integration pathway and the nature of the application, precise tuning of the interaction strength between 2D and 3D materials is required. As such intercalation at the graphene-metal interface has been widely studied as a means of tuning interaction strength.[18–22] Selective oxidation of the metal surface beneath graphene has been introduced as a route to weaken interaction and facilitate graphene transfer with minimised damage and contamination.[4,23–25] On the other hand, for applications where the 2D layer functions as a corrosion inhibitor[17,26,27] a strong graphene-metal interaction is required to suppress oxidation.[16] Thus, engineering the graphene-substrate interface is of crucial importance for many 2D material applications.

Here we study the influence of crystallographic orientation on the interaction and chemistry at the 2D-3D materials interface, specifically focussing on ambient oxidation at the buried graphene-Cu interface. Our model system is chemical vapour deposited (CVD) graphene on poly- and single-crystalline Cu substrates. There have been a large number of reports already on various aspects of the graphene/Cu interaction and the related Cu oxidation/corrosion behaviour. We therefore first summarise the salient points from these studies that we build on here, focussing particularly on room temperature conditions: for short time scales (minutes) graphene suppresses species reaching the Cu surface and thus protects Cu from corrosion in air and in corrosive liquids.[28–31] For longer time scales (hours to days) the presence of graphene can enhance corrosion due to galvanic corrosion.[23,29,32,33] For metals that interact strongly with graphene such that hybridisation of the band structure occurs, the intercalation of species at the buried interface is suppressed.[16] Whereas for comparatively weakly binding, such as graphene on Cu, intercalation of species can more readily proceed.[34,35] Isotope labelling studies have shown that under certain conditions the oxygen that forms the Cu oxide at the interface is from adsorbed water and not from the molecular oxygen in air,[23] with similar results found on Ru(0001) at cryogenic temperatures, where dissociated water intercalates but not O_2 or H_2.[36] The graphene/Cu interaction strength depends on the Cu crystal orientation as well as the epitaxial relationship, which leads to anisotropy in the Cu oxidation rate at the graphene/Cu interface for different Cu orientations.[25,37–40] Graphene on Cu(111) and Cu(311) can form an epitaxial system where the interaction of graphene and Cu is comparatively strong,[40–43] and the suppression of Cu surface oxidation seen for these systems has been attributed to this epitaxy.[37,40,44] Interestingly however, other Cu facets covered with non-commensurate graphene, such as Cu(124), have also been found to be relatively inert to oxidation.[25]

These previous studies on select graphene covered Cu facets motivate us here to systematically study ambient oxidation behaviour for over a hundred different (high and low index) Cu orientations. We employ complementary characterisation by electron backscatter diffraction (EBSD), high spatial resolution (submicrometer spot size) X-ray scanning photo-emission microscopy/microspectroscopy (SPEM, see Methods), Raman spectroscopy and atomic force microscopy (AFM). Across the whole polar plot of surface orientations, we identify four general oxidation modes and rationalise the

behaviour of each with respect to the underlying mechanisms, and then further discuss their relevance and generality.

Results

As a model substrate we use 1 mm thick, chemical mechanical polished (CMP), polycrystalline Cu (purity is 99.99 %) onto which without further pre-treatment graphene islands were synthesised by CVD (see Methods). In addition, we use single crystal Cu (111), (011) and (001) substrates. Note the Cu(111) sample recrystallized into higher index surfaces during the CVD conditions used here (see SI). The CVD process results in a graphene nucleation density of approximately 30 mm^{-2}, and using a growth time of 4 h leads to largely isolated graphene domains of roughly 250 µm in lateral size.[45] The graphene is predominantly mono-layer, as has been shown previously.[45] After the CVD process the lateral Cu grain dimensions of our model substrate are of the order of 1 mm, as shown by the electron backscatter diffraction (EBSD) map in Fig. 1(a). Highlighted by the inverse pole figure coloration, we find a range of different Cu surface orientations. The as-grown sample was stored in a class 10000 cleanroom for more than 2 years, with a controlled humidity level of 50% and temperature of 21 °C. Fig. 1(b) shows a corresponding optical microscope image. The observed contrast patterns highlight a very diverse, Cu facet dependent oxidation behaviour underneath and in between the graphene islands.

It is well known that a graphene coating can change the Cu oxidation behaviour, and this effect is widely used to optically characterise graphene coverage and defects.[37,46–49] The optical contrast and colour can thereby be linked to the Cu oxide thickness, ranging from metallic white (unoxidised) to yellow, orange and red with increasing thickness of the Cu oxide.[50–53] We verify the correlation between optical contrast and degree of Cu oxidation via a combination of X-ray photoelectron spectroscopy (XPS) microscopy, Raman spectroscopy and AFM. For XPS analysis the sample was annealed at 100 °C in vacuum to remove surface contamination. In order to structure these large data sets, we employ image processing and colour thresholding (see SI) on our optical microscopy data to extrapolate a quantitative parameter θ_{ox} that represents the extent of Cu oxidation based on areal coverage under graphene for a given Cu facet. We thereby only consider graphene covered areas, and for each crystallographic Cu orientation the θ_{ox} -value was averaged over all pixels, with $\theta_{ox} = \frac{Oxidised\ area\ under\ graphene}{Graphene\ covered\ area}$. The relative degree of oxidation of bare Cu areas, without graphene coverage, is characterised separately (see SI, Fig. S7).

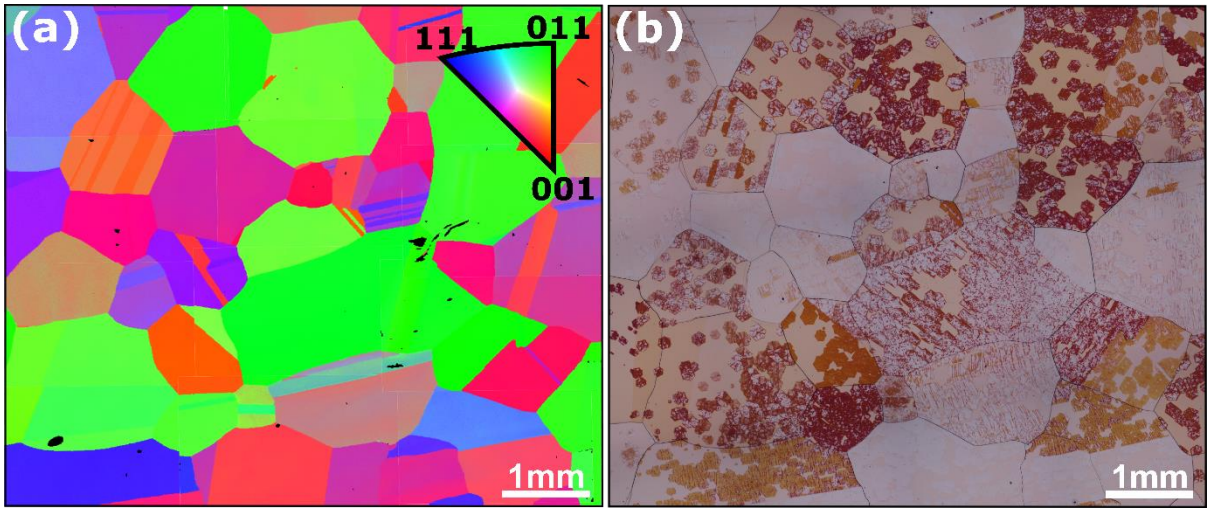

Figure 1: (a) Electron backscatter diffraction map (EBSD) of a polycrystalline Cu substrate after graphene CVD (see methods). The sample was stored in air for 2 years. The figure inset shows the inverse pole figure (IPF) colour code. (b) Corresponding optical microscope image. The observed colour contrast reflects the degree of oxidation for different Cu facets underneath and between the graphene islands.

Fig. 2 shows θ_{ox} plotted onto the corresponding inverse pole figure (IPF) and it reveals four distinct modes of graphene/Cu interface interaction. Cu orientations for which we observe the dominating influence of Cu/graphene corrugations/wrinkles on the oxidation are all marked with rhombuses. The data from {011} and {001} single crystal Cu substrates is shown by pentagons (see also SI Fig. S6). We find that our Cu(111) single crystal recrystallizes into different higher index orientations under the conditions used, therefore we were not able to verify the oxidation behaviour for this reference orientation. Instead, we include in Fig. 2 literature values marked with a star for the {111} orientation, which is reported not to cause interface oxidation even after extended air exposure.[40,44,54] On Cu facets close to {111} orientations, Cu oxidation occurs via a strong contribution from wrinkles. On Cu facets close to {011} orientations such wrinkle oxidation is not observed, and instead an irregular oxidation pattern appears under the graphene. Complete oxidation (i.e. θ_{ox} approaching 1) is found on Cu facets close to {001} orientations. For Cu facets close to {113} orientations there is a region where we find values of θ_{ox} close to 0, indicating that graphene completely inhibits Cu oxidation even after 2 years of air exposure. In the following we categorise these regions as “complete oxidation”, “irregular oxidation”, “inhibited oxidation” and “enhanced wrinkle oxidation”, as mapped out and labelled in Fig. 2. Data points representative of the oxidation behaviours of the four identified key interface characteristics are highlighted by black arrows in Fig. 2. In the following we focus on detailed characterisation of these representative points in order to develop an understanding of these distinct oxidation behaviours at the buried graphene/Cu interface.

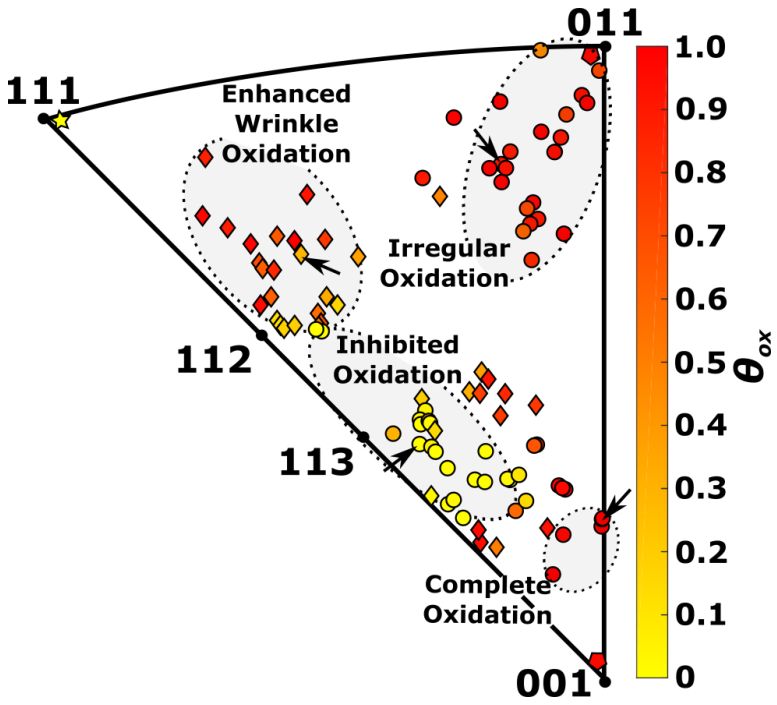

Figure 2: Extent of surface oxidation under graphene (θ_{ox}) for each Cu crystallographic orientation as computed by colour thresholding and EBSD analysis. Cu facets with strong influence of wrinkles on oxidation are shown with rhombus shape. Note in the case of fully oxidised ($\theta_{ox} = 1$) and for no oxidation ($\theta_{ox} = 0$) no rhombuses are assigned as wrinkles cannot be distinguished. {001} and {011} single crystal Cu substrates are shown by pentagons. The {111} orientation could not be verified here and we display literature values[40,44,54] with a star.

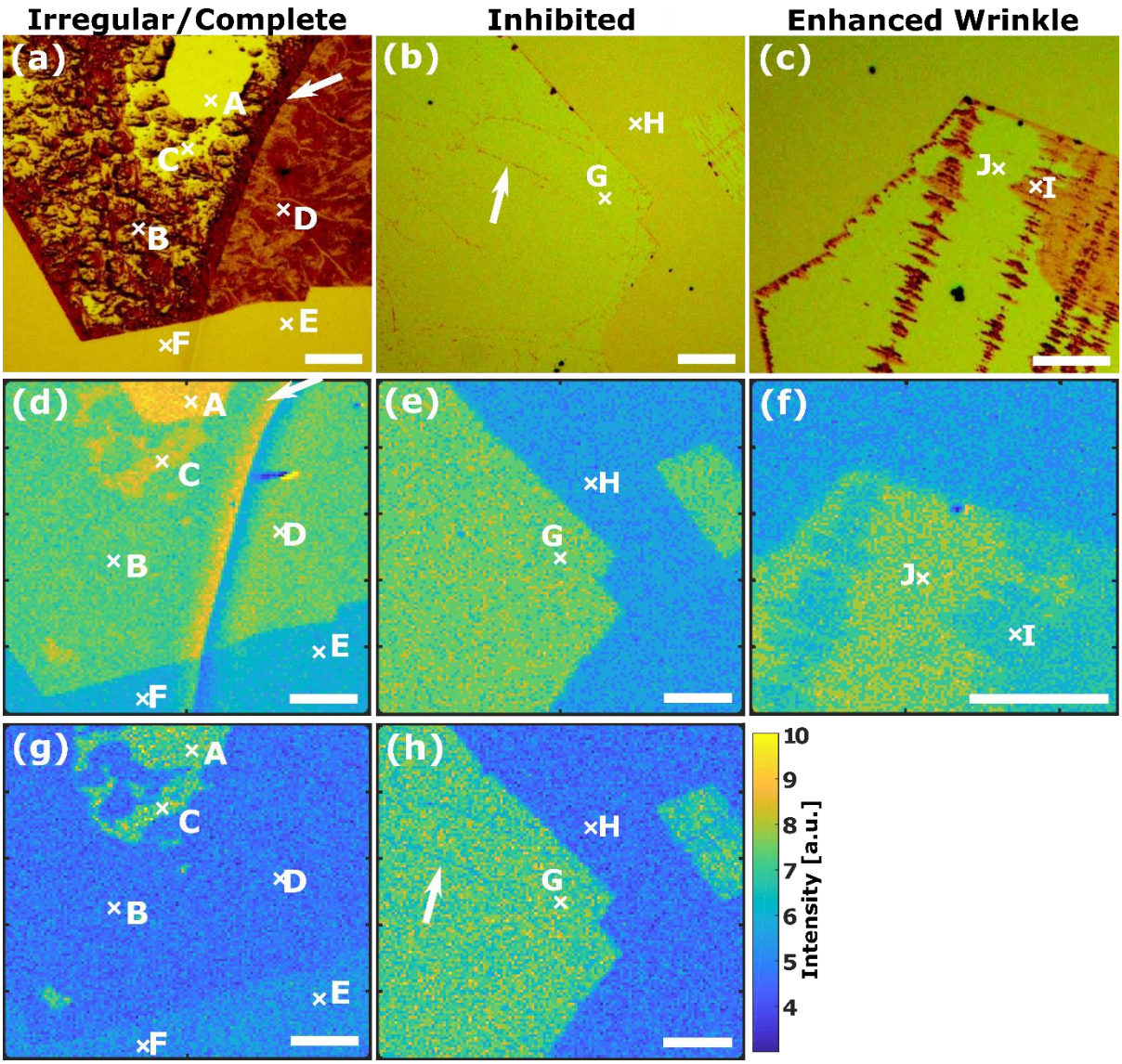

Figure 3: (a-c) Optical microscope images of the Cu substrate after CVD graphene synthesis and exposure to air for 2 years representative of the 4 regions indicated by arrows in Fig. 2. (a) "Irregular Oxidation" on the left side of the image separated by a Cu grain boundary marked by an arrow. The right side represents a "complete oxidation" region. (b) Area representing "inhibited oxidation" only few thin wrinkles (one marked by arrow) show oxidation while the remaining graphene covered area is unoxidized. (c) Area representing "enhanced wrinkle oxidation". The letters A-J mark locations were Raman and XPS spectra were taken. (d-f) SPEM intensity maps of the C 1s region for the areas shown in (a-c). (g-h) SPEM chemical contrast maps of the Cu LMM peak for locations shown in (a-b), higher intensity (green) indicates unoxidized Cu and lower intensity (blue) the oxidised state. All scale bars are 20 µm.

Fig. 3 shows higher resolution optical microscopy images (a-c) combined with spatially resolved, synchrotron source SPEM maps (d-h). The optical microscope data in Fig. 3(a-c) highlight that local phenomena influence the oxidation behaviour, which we will describe and characterise in detail in the following. Fig. 3(a) shows a graphene island that crosses a Cu grain boundary (highlighted by an arrow) and upon crossing of the Cu grain boundary the colour and homogeneity of the copper oxide changes. We observe this phenomenon across the entire sample and graphene islands that cross a Cu grain boundary show an oxidation pattern that is dominated by the underlying Cu surface orientation (for details see Fig. S1 and S2) and apparently rather independent of the graphene flake and its relative orientation to the underlying Cu. A brighter area in Fig. 3(a), marked by the letter 'A' which corresponds to a bilayer graphene region remained unoxidized [all other graphene covered regions in

Fig. 3 are monolayer graphene (see SI section 3)]. On the left side of the domain boundary in Fig. 3(a) Cu shows an area of "irregular oxidation", whereas on the right side a region of "complete oxidation" is shown. Fig. 3(b) shows bright contrast across all graphene covered regions corresponding to unoxidized Cu below the graphene layer except for narrow wrinkles with orange contrast. We label this as "inhibited oxidation". In strong contrast to the narrow wrinkles in Fig. 3(b), Fig. 3(c) shows parallel lines of dark red colour where enhanced oxidation is found, and the remaining graphene covered region appears brighter in optical contrast and unoxidized. We label this region "enhanced wrinkle oxidation". In Fig. 3(c) we observe that starting from a wrinkle the oxide preferentially grows anisotropically in the direction perpendicular to the wrinkle direction. Furthermore, the graphene island edges are also preferentially oxidised, and oxidation seems to proceed from the graphene island edge inwards, in agreement previous reports.[55,56]

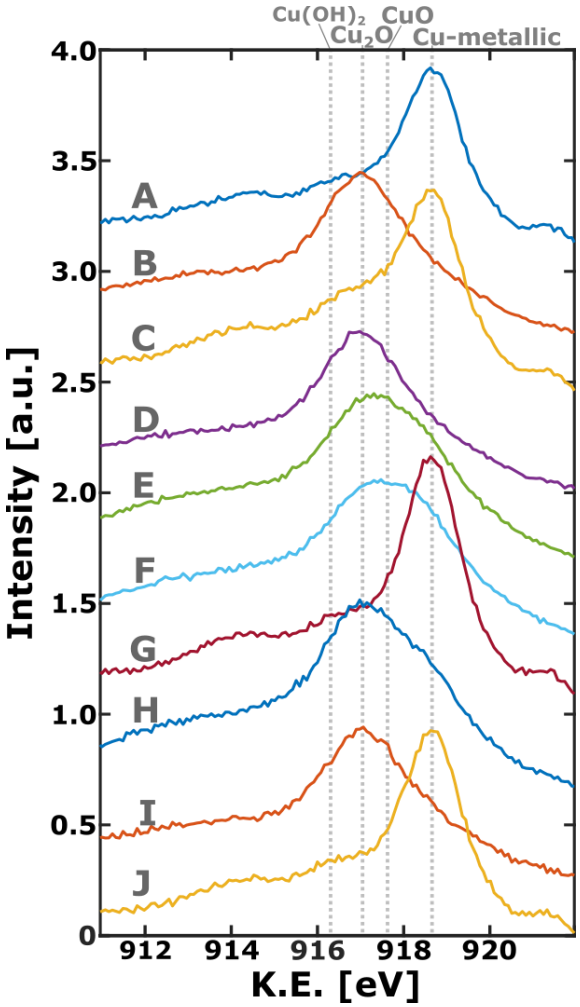

Figure 4: XPS Cu LMM Auger-Meitner spectra of locations A-J. As guide to the eye, the grey dotted lines mark the peak positions relating to the most intense Cu LMM peaks for metallic Cu, CuO, Cu_2O and $Cu(OH)_2$ (for peak fitting see Fig. S10).[57]

Conventional XPS with a spot size of several hundred µm is not suitable for resolving local oxidation behaviour as observed here. Therefore, to unequivocally determine the oxidation state of Cu under the graphene layer with a resolution small enough to resolve local effects such as wrinkles and Cu grain boundaries, we here use SPEM (see Methods) that has sub-micrometre spatial resolution. Fig. 3 (d-f) shows the C 1s intensity maps acquired at 285.3 eV binding energy corresponding to approximately the same locations as the optical images (Fig. 3a-c). A clear contrast is visible in the C1s

maps between the graphene-covered and uncovered areas. When measuring the C 1s signature on Cu and Cu_2O there is also a change in background intensity, resulting in the contrast seen in Fig. 3 (d-f). The reason for this is, that the Cu signals have a higher intensity in the case of metallic Cu which results in a higher number of secondary electrons and thus a higher background level at the C 1s peak position. At the Cu grain boundary in Fig. 3 (d) the signal intensity is increased which is not related to oxidation, but a topography artefact.

Since, there is only a small binding energy difference in the Cu $2p_{3/2}$ core level peak for metallic Cu and Cu_2O, we focus here on the Cu LMM Auger-Meitner signature which is more sensitive to changes in the Cu oxidation state.[34,58,59] Spatial mapping of the Cu LMM fingerprint region allows to obtain chemical contrast maps which show the ratio of metallic to oxidised Cu (more details see Methods). They are shown in Fig. 3(g-h) and confirm that locations in white in the optical microscope image match to a Cu LMM chemical contrast intensity corresponding to unoxidized regions.

The letters 'A'-'J' in Fig. 3 mark points were XPS and Raman point spectra were taken to fully characterise these locations. Upon exposure to air Cu mainly forms Cu_2O, CuO and $Cu(OH)_2$. Note that prior to the XPS measurement the sample was annealed at 100 °C in vacuum to remove surface contamination but which could also begin to reduce any CuO present to Cu_2O,[60] given its instability in vacuum.[61] Fig. 4 shows the Cu LMM spectra of locations 'A'-'J' and the peak positions of the most intense peak corresponding to Cu_2O, CuO and $Cu(OH)_2$, whose kinetic energies are shifted with respect to the metallic peak by -1.04 eV, -1.62 eV, -2.36 eV,[57] respectively. The Cu LMM signature is very complex, and in Fig. 4 we only mark the location of the most intense peak for the species indicated (for further details see Fig. S10). In line with the optical microscopy images, points 'A', 'C', 'G', 'J' show a Cu LMM spectra corresponding to unoxidized Cu, whereas the remaining spectra show Cu LMM spectra corresponding to oxidised Cu (peak fitting confirms this; see section 2 in the SI). Cu LMM peak fitting (see SI Fig. S10) reveals that the presence of a graphene overlayer alters the oxide composition. Graphene covered and oxidised regions 'B', 'D' and 'I' consist of only Cu_2O whereas locations 'E', 'F' and 'H' that correspond to graphene uncovered regions are composed of a mixture of Cu_2O and CuO. Location 'A' refers to a bilayer region and Fig. 4 shows that 'A' is unoxidized although the remaining Cu areas beneath monolayer regions of this graphene domain are oxidised. This highlights that bilayer graphene shows a very different interface oxidation behaviour compared to monolayer graphene.

Fig. 5 shows Raman mapping data corresponding to the same sample regions as in Fig. 3, performed to resolve the effect of Cu orientation and oxidation on the graphene doping concentration and strain. We present the Raman data as scatter plots of G peak wavenumber (ω_G) vs. 2D peak wavenumber (ω_{2D}) for the four key regions (Fig. 2), to highlight the different local strain (ε) and doping ($|n|$) concentrations.[13,62–64] The colour bar indicates the full width half maximum (FWHM) of the 2D peak, which is an indication of local strain homogeneity.[64] There is a clear trend in how the strain in the graphene relates to the Cu oxidation state irrespective of the Cu orientation. Oxidised Cu regions result in tensile strain ($\varepsilon > 0$) in the graphene layer (Fig. 5(a), (b) and some regions in (d)), whereas unoxidized regions are under compressive strain ($\varepsilon < 0$) ((Fig. 5(c), and parts of (d)). Irrespective of the Cu grain we observe a very wide spread in graphene strain that ranges approximately from $0 \lesssim \varepsilon \lesssim 0.8$ % on oxidised areas and from $-0.8 \lesssim \varepsilon \lesssim 0$ % on unoxidized areas. The graphene doping concentration also correlates with the underlying Cu oxidation state: in the case of "inhibited oxidation" we find the overall lowest doping concentration of approximately $|n| \cong$ ~0 – $0.5*10^{13}$ cm^{-2}. For "complete oxidation" $|n|$ appears to converge to a value of approximately $|n| \cong 1*10^{13}$ cm^{-2}, and for "irregular oxidation" $|n|$ is in-between the oxidised and unoxidized case and shows a larger spread from $|n| \cong$

~0 - 1*10^{13} cm^{-2}. This is in line with the C 1s spectra provided in Fig. S9, where a change in the level of charge transfer between the Cu and graphene results in a binding energy shifts of the C 1s core level. Here, a shift towards higher binding energies of approx. 0.15 - 0.25 eV suggesting n-type doping for locations 'A',' B', 'C', 'D' and 'I' is observed but no binding energy shift is observed for position 'G' and only a small shift of approx. 0.05 - 0.1 eV for location 'J'.

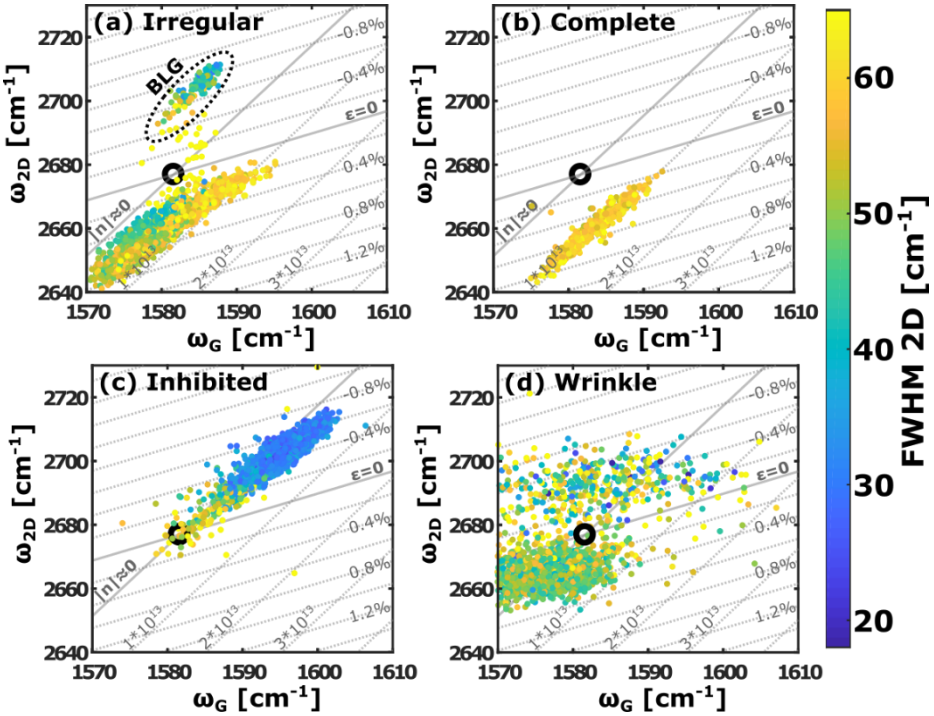

Figure 5: Scatter plot of G peak position (ω_G) and 2D peak position (ω_{2D}) as well as the full width half maximum (FWHM) of the 2D peak indicated by colour. ε refers to strain in % and $|n|$ to the carrier concentration in cm^{-2}. (a) Refers to the data acquired at the region "irregular oxidation", the data points labelled BLG correspond to the bilayer graphene region, (b) to the region "complete oxidation", (c) to the region "inhibited oxidation" and (d) to the region "enhanced wrinkle oxidation".

We further note that the Cu crystallographic dependent oxidation behaviour described above is not limited to graphene islands, but the same Cu grain dependent oxidation behaviour is observed for samples with full graphene coverage (see SI Fig. S18). Furthermore, the results presented here are not limited to CMP polished Cu substrates but equally apply to cold rolled thin (25 µm) Cu foils that are substantially rougher (R_a ~ 300 nm).[45] SI Fig. S19 shows that Cu grain dependent oxidation behaviour following the 4 different oxidation categories identified in Fig. 2 is also observed on these rough cold rolled Cu foils on which graphene was grown and which were exposed to air.

Whereas our study primarily focuses on the oxidation at the graphene/Cu interface under ambient conditions, we also performed a wet oxidation treatment to investigate the Cu orientation dependence under such different, comparatively more harsh conditions.[23,65] In order to use the same sample the Cu interface oxidation was reduced by hydrogen annealing.[34] Annealing for 3h at 250°C and 5 mbar H_2 reduces the oxide at the graphene Cu interface (see SI section 5).[34,35] After reduction we immerse the Cu/graphene sample in de-ionized water at 50 °C for 3 days, which causes wet-oxidation of the graphene/Cu interface.[4] In contrast to the above described oxidation in ambient conditions, the microscope colour contrast shows that wet oxidation at these conditions leads to uniform oxidation across all Cu crystallographic orientations (see SI section 5). Compared to oxidation in air, interface oxidation in water is significantly accelerated.[23,66,67] Furthermore, Raman spectroscopy

analysis shows very low residual strain after water oxidation compared to air oxidation and in the case of water oxidation also graphene bilayer regions can be intercalated and oxidised.

Discussion

The results herein show that for the graphene-Cu interface there are several effects that influence the interface oxidation behaviour and these effects are strongly linked to the Cu surface orientation. The characteristic oxidation patterns observed can be associated with regions in the IPF plot rather than discrete Cu orientations (Fig. 2). Based on this we can exclude epitaxial effects between graphene and the underlying Cu as a major influence on the observed oxidation behaviour. Furthermore, Fig. 3(a) (see also Fig. S1) shows that if a graphene island crosses a Cu grain the oxidation pattern drastically changes at the Cu grain boundary to resemble that of the other islands on the new Cu grain, which indicates that the underlying Cu is the dominating factor in oxidation rather than a particular graphene orientation relative to the Cu. The dark red colour in the optical microscope images indicates that some areas under the graphene develop a thicker Cu-oxide compared to the bare Cu surface, hinting at a galvanic corrosion mechanism.[23,29,32,33] Galvanic corrosion is driven by a work function difference between graphene and Cu. The work function of Cu is highly dependent on the Cu surface.[68–71] In a simple model the work function of a surface is directly correlated to the step density where the steps add additional dipoles moments to the edge atoms (see also 'Smoluchowski-effect'[72]) i.e. the work function decreases with increasing step density {111}(4.7 eV)>{100}(4.5 eV)>{211}(4.5 eV)>{123}(4.4 eV)>{110}(4.3 eV)>{310}(4.3 eV).[73] The work function of (undoped) graphene is around 4.5 eV.[74–76] Hence, if a surface, for example the {111}, {100} and {211} orientations, have a work function higher or equal to graphene no galvanic corrosion would be expected in this simplified model. In contrast if the work function of the Cu surface is lower than the work function of graphene e.g. vicinals of the {110} orientation, galvanic corrosion effects are expected. Indeed, the overall picture in Fig. 2 resembles some of these trends i.e. vicinals of the {111} orientation with the highest work function mostly show oxidation along the wrinkles but no oxidation in unwrinkled areas (see Fig. 3 c,f) and the inhibited oxidation region corresponds to an area with work function of approximately 4.5 eV. Vicinals of the {110} orientation have relatively lower work functions and we indeed see increased oxidation including the complete oxidation region, consistent with galvanic corrosion. Further evidence for this argument is that the acquired Raman spectra on areas corresponding to the “inhibited oxidation” region of the IPF do not show doping effects (see Fig. 5(c)), indicating negligible between the Cu and graphene work functions. This is also the case after water oxidation (see Fig. S17(b)). We note that the graphene covered surfaces shown in AFM maps of Fig. S13 have a surface roughness (R_a) ranging from approximately 5 to 20 nm. The Cu work function decreases with increasing surface roughness and therefore the actual surface work function will be a convolution of the surface roughness and facet specific work function.[77] Also note that the electron beam penetration depth used for EBSD here is on the order of 50-100 nm.[78] Therefore, the graphene layer may locally be in contact with a range of other surface facets due to the surface roughness and surface reconstructions that are not captured by the EBSD measurement.[79] Nevertheless, there is a strong correlation of the interface oxidation behaviour to the EBSD measured surface orientation despite the graphene layer being in contact with a rough surface. This not only holds for the flat samples used here but also for comparatively rough ($R_a \approx 300$nm)[45] Cu foils (see Fig. S18). Further evidence for the strong contribution of galvanic corrosion are comparative studies of insulating hexagonal boron nitride (h-BN) monolayers on Cu, which are

shown to be better long term corrosion barriers than graphene, as insulating h-BN layer cannot drive galvanic effects.[80–82]

Assuming a defect free graphene layer is impermeable to gas molecules,[83,84] for oxidation to occur oxygen species must intercalate beneath the graphene layer to react with the underlying Cu surface. We do not detect a Raman D peak away from the edges of the graphene domains on any Cu orientation (see Fig. S11), however defect densities (n_D) on the order of less than $n_D \approx 5$ μm^{-2} on Cu substrates are very challenging to resolve with Raman.[85] Therefore, for Cu oxidation to occur under graphene oxygen species need to diffuse through the graphene layer via defects or intercalate via the edges. For oxidation to proceed, the diffusion pathway must remain active and not be self-passivating upon oxidation. Additional AFM images in the SI (see Fig. S13) show that there is no obvious correlation between surface roughness and the oxidation behaviour with the exception of wrinkles (Fig. S13(f-g)). The areas under the graphene wrinkles are oxidised, which indicates that the Cu-graphene interaction is weakened in these areas and oxygen species can more easily penetrate the interface here. For the Cu grains classified as "enhanced wrinkle oxidation" (Fig. S13(f-g)) we also observe a regular surface corrugation pattern on unoxidized areas, and these corrugations are perpendicular to wrinkles. The surface corrugations correlate to the anisotropic oxide growth rate that is observed in direction of the corrugation and may be explained by an accelerated oxide species diffusion rate along the corrugation compared to oxide diffusion across the corrugation. These surface corrugation have previously been described as Cu step bunches.[86] The existence of such Cu step bunches, wrinkle formation and variations in strain are commonly rationalised via a thermal expansion coefficient mismatch between graphene and Cu. The thermal expansion coefficient mismatch causes the graphene film to be under compressive stress and the Cu surface layer to be under tensile stress.[43,86–90] The Cu surface can be considered as highly mobile or "pre-molten" at the CVD conditions used, however such pre-melting behaviour is also dependent on the Cu crystallographic orientation.[91] Upon cooling the tensile stress in the Cu surface layer is relaxed by the formation of step bunches.[86] The compressive strain in graphene is relaxed by out of plane wrinkle formation, which again is dependent on the Cu crystallographic interaction strength of the graphene-Cu interface.[43,86–90] This is consistent with our measurements in Fig. 5(d) (see also Fig. S11 and S12), where we observe reduced strain along a graphene wrinkle. Upon intercalation and interface oxidation there is a volume expansion due to Cu oxidation and thus the compressive strain in graphene is released and graphene is under tensile strain (see Fig. 5). Previous reports describe how such Cu corrugations can relax in graphene wrinkles which occur perpendicular to the Cu surface corrugation.[86] Corrugations perpendicular to wrinkles are consistent with our observation in Fig. S13. Previous reports also observed oxidation along wrinkles for orientations close to Cu {111} and {001} but not on surfaces closest to {011}, which is in line with our findings.[92] Indeed, the Cu thermal expansion coefficient is dependent on the Cu crystal orientation but these differences in thermal expansion coefficient are relatively small.[93]

Fig. S13 shows how different graphene covered Cu orientations reconstruct and as a result the surface roughness becomes markedly different. Differences in surface roughness can have notable effects on the hydrophobicity of a surface and thereby drastically change the oxidation rates.[94–98] It is well known that hydrophobic Cu surfaces exhibit increased corrosion protection when exposed to atmospheric conditions.[99] Furthermore, water diffusion at the graphene substrate interface was shown to be significantly increased by increasing the hydrophilicity of the substrate.[100] However, the fact that we observe similar surface roughness for the "inhibited oxidation" and "complete oxidation" case hints that the difference is not pronounced when Cu is stored in air. However, prolonged immersion in

water at 50 °C eventually leads to oxidation on all surface orientations (see SI section 5), in line with previous reports that have shown accelerated oxidation rates in water.[23,66,67] By isotope labelling Luo et al.[23] have shown that water, not oxygen species from air are the main contributor to the interface oxide. Our data is consistent with this. An acceleration of the oxidation rate can be obtained by supplying water vapour or by immersion in water.

While above has focussed on graphene covered Cu, it is also known that the oxidation rate varies with surface orientation for bare Cu.[101–106] The oxidation rate of a bare Cu surface correlates with the surface step density during the initial phase of oxidation and therefore an orientation dependent oxide formation rate is expected.[101–104] However, the subsequent oxide growth process is complex and depends on various factors that cannot be solely explained by the surface step density.[105,106] Fig. 1(b) shows an orientation dependent colour contrast also for bare Cu regions. The relative orientation dependent oxide rate is further quantified in Fig. S7(b) and mapped in an IPF plot in similar fashion to Fig. 2. Comparing Fig. 2 and Fig. S7(b), a strong correlation between the oxidation behaviour of graphene covered and bare Cu regions is observed. The orientations that are marked as inhibited oxidation under graphene in Fig. 2 also show relatively low oxidation for bare Cu regions. Orientations with irregular and complete oxidation under graphene also show the highest degree of oxidation for bare Cu regions (see Fig. S7(b)). A notable difference in oxidation extend are the "enhanced wrinkle" orientations, where without the presence of graphene a relatively low degree of oxidation is observed. This highlights the argument above, that wrinkles enable oxygen species to diffuse and cause oxidation locally. Whereas graphene covered and bare Cu oxidation mostly show a similar trend when comparing patterns across the IPF, the oxide thickness and oxide composition are distinctly different. Our XPS data shows that a graphene layer changes the Cu oxide composition and underneath graphene only Cu_2O is observed, whereas bare Cu regions are composed of a mixture of CuO and Cu_2O (see Fig. S9 and S10).[55] Previous reports have shown that when Cu is exposed to air, CuO is only observed at the surface in direct contact with the atmosphere and a thicker Cu_2O layer is found underneath the CuO layer.[107] Thus, for graphene covered oxide regions the graphene layer is protecting the Cu_2O layer from contact with the atmosphere and therefore prevents the Cu_2O layer from further oxidising to CuO. We here focus on monolayer graphene films, but note that for areas covered with bilayer graphene, no Cu oxidation is observed at ambient conditions (see Fig. 3 a,d,g). Mismatched defects between the layers in bilayer graphene hinder diffusion of oxygen species in the vertical direction compared to monolayer graphene.[108] Furthermore, we do not observe wrinkles in the bilayer region (see Fig. S13 c), which when present provide additional pathways for oxygen species to access the Cu surface. This may explain why we do not observe oxidation under bilayer graphene (see Fig. 3 a,d,g), even on a Cu orientation where otherwise higher oxide coverages are observed. However, in more corrosive oxidation environments e.g. by water immersion (50 °C for 3 days) even bilayer regions become oxidised (see Fig. S15(*)). This suggests that bilayer graphene does not offer a different corrosion protection mechanism beyond fewer penetration pathways for oxygen species, as eventually the oxidation front will intercalate from the graphene island edges inwards irrespective of defect density.

Conclusion

We have synthesised graphene islands on flat polycrystalline Cu substrates with a range of different Cu orientations. After exposure to ambient conditions for 2 years Cu grain orientation dependent oxidation was observed that can be classified as complete-, irregular-, inhibited and enhanced wrinkle

-interface oxidation. The characteristic oxidation patterns observed are associated to regions in the IPF plot rather than discrete Cu orientations (see Fig. 2). Our results clearly demonstrate that under ambient conditions the Cu orientation is the dominant factor in determining the oxidation behaviour under graphene as our experimental design accounts for factors such as surface roughness, different growth conditions, and different graphene quality on each domain, allowing these to be excluded. We expect the observed classification to be relevant to different oxidising environments, such as saturated water vapour now widely used for graphene transfer. Indeed, our generalised groupings and mapping onto the polar plot of Cu surface orientations consistently consolidates a large body of previous literature on select individual Cu orientations, all under slightly different conditions. Our example of immersion in water, however, shows that for very corrosive conditions ultimately all Cu orientations can be oxidised underneath the graphene (mono- or bi-layer), i.e. the described Cu orientation dependent effects should be understood with respect to given exposure conditions. Recent reports have demonstrated the production of high and low index Cu foils with desired orientation,[109] which enables the findings of this paper to be translated beyond individual grains. We expect our study to facilitate future optimisation of process technology tailored to diverse emerging application needs for graphene and other 2D materials that face analogous challenges, ranging from complete and uniform intercalation and interface oxidation as required for example for optimised 2D layer transfer to complete oxidation protection by an atomic monolayer for instance for plasmonics.

Methods

Chemical mechanical polished (CMP), polycrystalline Cu metallic substrate (dimensions 1 × 10 × 10 mm^3) as well as single crystals with orientation (111), (011) and (001) were used as graphene growth substrate. According to distributor specifications (PiKem Limited) the Cu purity is 99.99 % and the surface roughness is R_a < 3 nm.

CVD was performed in a commercial Aixtron Black Magic 4'' system. The Cu substrate was loaded into the CVD system without further surface treatment. CVD synthesis was performed by heating in Ar atmosphere at 100 °C/min to 1065 °C. The sample was annealed for 30 min which leads to Cu grain growth for the polycrystalline substrates, followed by carbon precursor injection (gas flow rates Ar:H2:CH_4 (0.1% diluted in Ar)= 250 sccm: 26 sccm: 12 sccm) for a growth time of 4 h after which the heaters were switched off and the chamber was cooled to room temperature in an Ar atmosphere.[45] During all process steps the chamber pressure was 50 mbar.

After synthesis the Cu substrate was stored in a class 10'000 cleanroom atmosphere for 2 years. The temperature of the cleanroom was regulated to 21 °C and the air humidity was regulated to 50 %.

The model system employed here allows us to rule out a series of uncertainties. Unlike commonly used cold rolled Cu foils for graphene synthesis we used polished Cu substrate to rule out surface roughness induced effects on oxidation. Analysing graphene islands which have previously been established to be predominantly single graphene domains[45] we can rule out the effect of graphene domain boundary induced defects as pathways for intercalation of oxygen species,[46,110] or sites for enhanced dissociation of intercalating species.[36] Furthermore, a Cu sample which is only partially covered with graphene islands allows direct comparison between the oxidation rate of the uncovered and graphene-covered areas. Using a single polycrystalline substrate rather than a series of single crystalline substrates ensures that the growth conditions were equal on all Cu grains as gas flux and temperature dependence can be assumed to be negligible over the 1 cm^2 sample area in a 4'' cold wall showerhead CVD reactor.[111] At the growth conditions used here CVD graphene defect densities

are on a similar order for all Cu grains[112] and further we can observe graphene single domain islands that cross Cu grain boundaries to clearly show the effect of underlying Cu orientation.

Raman analysis was performed in a Renishaw inVia Raman microscope with a 532 nm laser with 100× objective and a 1800 l/mm grating. Scanning electron microscopy (SEM) analysis was performed using a Carl Zeiss SIGMA VP at an acceleration voltage of 2 kV.

The EBSD was conducted on a FEI Nova NanoSEM scanning electron microscope with an acceleration voltage of 20 kV. The sample was tilted at 70 ° towards the EBSD detector, which was approximately 20 mm from the surface of the sample. The contrast and the background subtraction of the electron backscatter diffraction patterns were optimized to maximize signal strength prior to each mapping measurement. Multiple maps were taken and later stitched together to form the image maps used in this work.

Scanning X-ray PhotoElectron Microscopy/microspectroscopy (SPEM) measurements were carried out at the Escamicroscopy beamline of the Elettra synchrotron facility (Trieste, Italy).[113] Samples were first annealed in vacuum to ~100 °C to remove residual surface contamination that otherwise obscures the signal from the Cu/graphene interface, with the temperature chosen to avoid significant changes to the Cu oxidation state[60] – though the instability of CuO may lead to its partial reduction to Cu_2O particularly under X-ray irradiation.[61] The X-ray beam was focused to a ∼180-200 nm spot by a Fresnel zone plate based optics.

For both imaging and submicron spectroscopy, a SPECS-PHOIBOS 100 hemispherical electron energy analyser with an in-house customized 48 channel delay line detector was used.[114] A photon energy of 1074 eV was employed. The SPEM can mainly work in two mode: (i) microspectroscopy mode i.e. the typical energy scanning mode employed in any standard XPS system, using a 180-200 nm X-ray spot size, and (ii) imaging mode can map the photoelectrons emitted within a selected kinetic energy window by scanning the specimen with respect to the focused X-ray beam. In the imaging mode each channel of the detector corresponds to slightly different energy resulting in a 48 data points spectrum at each pixel. All binding energies are referenced to the Cu 2p peak energy which was set to be 932.6 eV. This approach is feasible on our sample because there is only a modest change between the metallic Cu and Cu_2O peak position and only small amounts of CuO are present.[59] To acquire the map of the C 1s peak in Fig. 3 (d-f) the energy window of the analyser was centred at a binding energy of 285.3 eV and for the Cu LMM it was set to the kinetic energy of 917.0 eV. To obtain the Cu LMM chemical contrast maps shown in Fig. 3(g-h) the integral ratio of the spectral regions containing mainly metallic (918.1 eV - 919.9 eV) and oxidized (915.8 eV - 918.1 eV) contributions was calculated and plotted for each pixel.

Supporting Information

Additional optical microscope and EBSD data, details on approach for colour thresholding, additional XPS, Raman and AFM data, details and characterisation of water oxidised samples and oxidation characteristics of additional samples.

Acknowledgements

We acknowledge financial support from the EPSRC (Grant No. EP/T001038/1 and EP/P005152/1). P.B.W. acknowledges EPSRC Cambridge NanoDTC Grant No. EP/G037221/1. O.J. B. acknowledges an EPSRC Doctoral Training Award (EP/M508007/1). R.S.W. acknowledges a EU Marie Skłodowska-Curie

Individual Fellowship (Global) under grant ARTIST (No. 656870) from the European Union's Horizon 2020 research and innovation programme.
We acknowledge the Elettra Sincrotrone Trieste storage ring for provision of synchrotron radiation under proposal 20165323 at the Escamicroscopy beamline and thank the Elettra staff for continuous support of our experiments.

References

(1) Chen, M.; Haddon, R. C.; Yan, R.; Bekyarova, E. Advances in Transferring Chemical Vapour Deposition Graphene : A Review. *Mater. Horizons* **2017**, *4* (6), 1054–1063.
(2) Banszerus, L.; Schmitz, M.; Engels, S.; Dauber, J.; Oellers, M.; Haupt, F.; Watanabe, K.; Taniguchi, T.; Beschoten, B.; Stampfer, C. Ultrahigh-Mobility Graphene Devices from Chemical Vapor Deposition on Reusable Copper. *Sci. Adv.* **2015**, *1* (6), 1500222.
(3) Wang, Y.; Zheng, Y.; Xu, X.; Dubuisson, E.; Bao, Q.; Lu, J.; Loh, K. P. Electrochemical Delamination of CVD-Grown Graphene Film: Toward the Recyclable Use of Copper Catalyst. *ACS Nano* **2011**, *5* (12), 9927–9933.
(4) Wang, R.; Whelan, P. R.; Braeuninger-Weimer, P.; Tappertzhofen, S.; Alexander-webber, J. A.; Van-veldhoven, Z. A.; Kidambi, P. R.; Jessen, B. S.; Booth, T. J.; Boggild, P.; et al. Catalyst Interface Engineering for Improved 2D Film Lift-Off and Transfer. *ACS Appl. Mater. Interfaces* **2016**, *8* (48), 33072–33082.
(5) Wang, R.; Purdie, D. G.; Fan, Y.; Massabuau, F. C.; Braeuninger-Weimer, P.; Burton, O. J.; Blume, R.; Schloegl, R.; Lombardo, A.; Weatherup, R. S.; et al. A Peeling Approach for Integrated Manufacturing of Large Monolayer H-BN Crystals. *ACS Nano* **2019**, *13* (2), 2114–2126.
(6) Giovannetti, G.; Khomyakov, P. A.; Brocks, G.; Karpan, V. M.; Brink, J. Van Den; Kelly, P. J. Doping Graphene with Metal Contacts. *Phys. Rev. Lett.* **2008**, *101* (2), 026803.
(7) Giubileo, F.; Di, A. Progress in Surface Science The Role of Contact Resistance in Graphene Field-Effect Devices. *Prog. Surf. Sci.* **2017**, *92* (3), 143–175.
(8) Hsu, A.; Wang, H.; Kim, K. K.; Kong, J.; Palacios, T. Impact of Graphene Interface Quality on Contact Resistance and RF Device Performance. *IEEE ELECTRON DEVICE Lett.* **2011**, *32* (8), 1008–1010.
(9) Yankowitz, M.; Ma, Q.; Jarillo- Herrero, P.; LeRoy, B. J. Van Der Waals Heterostructures Combining Graphene and Hexagonal Boron Nitride. *Nat. Rev. Phys.* **2019**, *1* (2), 112–125.
(10) Martin, M. B.; Dlubak, B.; Weatherup, R. S.; Piquemal-Banci, M.; Yang, H.; Blume, R.; Schloegl, R.; Collin, S.; Petroff, F.; Hofmann, S.; et al. Protecting Nickel with Graphene Spin-Filtering Membranes: A Single Layer Is Enough. *Appl. Phys. Lett.* **2015**, *107* (1), 012408.
(11) Alexander-Webber, J. A.; Sagade, A. A.; Aria, A. I.; Van Veldhoven, Z. A.; Braeuninger-Weimer, P.; Wang, R.; Cabrero-Vilatela, A.; Martin, M.-B.; Sui, J.; Connolly, M. R.; et al. Encapsulation of Graphene Transistors and Vertical Device Integration by Interface Engineering with Atomic Layer Deposited Oxide. *2D Mater.* **2017**, *4* (1), 011008.
(12) Dlubak, B.; Martin, M.-B.; Weatherup, R. S.; Yang, H.; Deranlot, C.; Blume, R.; Schloegl, R.; Fert, A.; Anane, A.; Hofmann, S.; et al. Graphene-Passivated Nickel as an Oxidation- Resistant Spin Polarized Electrode. *ACS Nano* **2012**, *6* (12), 10930–10934.
(13) Banszerus, L.; Janssen, H.; Otto, M.; Epping, A.; Taniguchi, T.; Watanabe, K.; Beschoten, B.; Neumaier, D.; Stampfer, C. Identifying Suitable Substrates for High-Quality Graphene-Based Heterostructures. *2D Mater.* **2017**, *4* (2), 025030.
(14) Akinwande, D.; Huyghebaert, C.; Wang, C.; Serna, M. I.; Goossens, S.; Li, L.; H.-S. Philip Wong; Koppens, F. H. L. Graphene and Two-Dimensional Materials for Silicon Technology. *Nature* **2019**, *573*, 507–518.
(15) Li, L.; Chen, X.; Wang, C.; Cao, J.; Lee, S.; Tang, A.; Ahn, C.; Roy, S. S.; Arnold, M. S.; Wong, H.

P. Vertical and Lateral Copper Transport through Graphene Layers. *ACS* **2015**, *9* (8), 8361--8367.
(16) Weatherup, R. S.; D'Arsié, L.; Cabrero-Vilatela, A.; Caneva, S.; Blume, R.; Robertson, J.; Schloegl, R.; Hofmann, S. Long-Term Passivation of Strongly Interacting Metals with Single-Layer Graphene. *J. Am. Chem. Soc.* **2015**, *137* (45), 14358–14366.
(17) Bohm, S. Graphene against Corrosion. *Nat. Nanotechnol.* **2014**, *9* (10), 741–742.
(18) Sutter, P.; Sadowski, J. T.; Sutter, E. A. Chemistry under Cover: Tuning Metal-Graphene Interaction by Reactive Intercalation. *J. Am. Chem. Soc.* **2010**, *132* (23), 8175–8179.
(19) Varykhalov, A.; Sánchez-Barriga, J.; Shikin, A. M.; Biswas, C.; Vescovo, E.; Rybkin, A.; Marchenko, D.; Rader, O. Electronic and Magnetic Properties of Quasifreestanding Graphene on Ni. *Phys. Rev. Lett.* **2008**, *101* (15), 1–4.
(20) Lizzit, S.; Larciprete, R.; Lacovig, P.; Dalmiglio, M.; Orlando, F.; Baraldi, A.; Gammelgaard, L.; Barreto, L.; Bianchi, M.; Perkins, E.; et al. Transfer-Free Electrical Insulation of Epitaxial Graphene from Its Metal Substrate. Suplemmentary Information. *Nano Lett.* **2012**, *12* (9), 4503–4507.
(21) Larciprete, R.; Ulstrup, S.; Lacovig, P.; Dalmiglio, M.; Bianchi, M.; Mazzola, F.; Hornekær, L.; Orlando, F.; Baraldi, A.; Hofmann, P.; et al. Oxygen Switching of the Epitaxial Graphene À Metal Interaction. *ACS Nano* **2012**, *6* (11), 9551–9558.
(22) Grüneis, A.; Vyalikh, D. V. Tunable Hybridization between Electronic States of Graphene and a Metal Surface. *Phys. Rev. B* **2008**, *77* (19), 193401.
(23) Luo, D.; You, X.; Li, B.-W.; Chen, X.; Park, H. J.; Jung, M.; Ko, T. Y.; Wong, K.; Yousaf, M.; Chen, X.; et al. Role of Graphene in Water-Assisted Oxidation of Copper in Relation to Dry Transfer of Graphene. *Chem. Mater.* **2017**, *29* (10), 4546–4556.
(24) Whelan, P. R.; Jessen, B. S.; Wang, R.; Luo, B.; Stoot, A. C.; Mackenzie, D. M. A.; Braeuninger-Weimer, P.; Jouvray, A.; Prager, L.; Camilli, L.; et al. Raman Spectral Indicators of Catalyst Decoupling for Transfer of CVD Grown 2D Materials. *Carbon* **2017**, *117*, 75–81.
(25) Lu, A.-Y.; Wei, S.-Y.; Wu, C.-Y.; Hernandez, Y.; Chen, T.-Y.; Liu, T.-H.; Pao, C.-W.; Chen, F.-R.; Li, L.-J.; Juang, Z.-Y. Decoupling of CVD Graphene by Controlled Oxidation of Recrystallized Cu. *RSC Adv.* **2012**, *2* (7), 3008.
(26) Kang, C. G.; Lim, S. K.; Lee, S.; Lee, S. K.; Cho, C.; Lee, Y. G.; Hwang, H. J.; Kim, Y.; Choi, H. J.; Choe, S. H.; et al. Effects of Multi-Layer Graphene Capping on Cu Interconnects. *Nanotechnology* **2013**, *24* (11), 115707.
(27) Li, L.; Wong, H.-S. P. Integrating Graphene into Future Generations of Interconnect Wires. *2018 IEEE Int. Electron Devices Meet.* **2018**, 5--5.
(28) Chen, S.; Brown, L.; Levendorf, M.; Cai, W.; Ju, S. Y.; Edgeworth, J.; Li, X.; Magnuson, C. W.; Velamakanni, A.; Piner, R. D.; et al. Oxidation Resistance of Graphene-Coated Cu and Cu/Ni Alloy. *ACS Nano* **2011**, *5* (2), 1321–1327.
(29) Schriver, M.; Regan, W.; Gannett, W. J.; Zaniewski, A. M.; Crommie, M. F.; Zettl, A. Graphene as a Long-Term Metal Oxidation Barrier: Worse than Nothing. *ACS Nano* **2013**, *7* (7), 5763–5768.
(30) Prasai, D.; Tuberquia, J. C.; Harl, R. R.; Jennings, G. K.; Bolotin, K. I. Graphene: Corrosion-Inhibiting Coating. *ACS Nano* **2012**, *6* (2), 1102–1108.
(31) Singh Raman, R. K.; Chakraborty Banerjee, P.; Lobo, D. E.; Gullapalli, H.; Sumandasa, M.; Kumar, A.; Choudhary, L.; Tkacz, R.; Ajayan, P. M.; Majumder, M. Protecting Copper from Electrochemical Degradation by Graphene Coating. *Carbon* **2012**, *50* (11), 4040–4045.
(32) Zhou, F.; Li, Z.; Shenoy, G. J.; Li, L.; Liu, H. Enhanced Room-Temperature Corrosion of Copper in the Presence of Graphene. *ACS Nano* **2013**, *7* (8), 6939–6947.
(33) Zahran, R. R.; Ibrahim, I. H. M.; Sedahmed, G. H. The Corrosion of Graphite/Copper Composites in Different Aqueous Environments. *Mater. Lett.* **1996**, *28* (1–3), 237–244.
(34) Kidambi, P. R.; Bayer, B. C.; Blume, R.; Wang, Z.-J.; Baehtz, C.; Weatherup, R. S.; Willinger, M.-G.; Schloegl, R.; Hofmann, S. Observing Graphene Grow: Catalyst-Graphene Interactions

during Scalable Graphene Growth on Polycrystalline Copper. *Nano Lett.* **2013**, *13* (10), 4769–4778.
(35) Blume, R.; Kidambi, P. R.; Bayer, B. C.; Weatherup, R. S.; Wang, Z.-J.; Weinberg, G.; Willinger, M.-G.; Greiner, M.; Hofmann, S.; Knop-Gericke, A.; et al. The Influence of Intercalated Oxygen on the Properties of Graphene on Polycrystalline Cu under Various Environmental Conditions. *Phys. Chem. Chem. Phys.* **2014**, *16* (47), 25989–26003.
(36) Feng, X.; Maier, S.; Salmeron, M. Water Splits Epitaxial Graphene and Intercalates. *J. Am. Chem. Soc.* **2012**, *134* (12), 5662–5668.
(37) Kwak, J.; Jo, Y.; Park, S. D.; Kim, N. Y.; Kim, S. Y.; Shin, H. J.; Lee, Z.; Kim, S. Y.; Kwon, S. Y. Oxidation Behavior of Graphene-Coated Copper at Intrinsic Graphene Defects of Different Origins. *Nat. Commun.* **2017**, *8* (1), 1–12.
(38) Jo, M.; Lee, H. C.; Lee, S. G.; Cho, K. Graphene as a Metal Passivation Layer: Corrosion-Accelerator and Inhibitor. *Carbon* **2017**, *116*, 232–239.
(39) Xu, Y.; Qu, J.; Shen, Y.; Feng, W. Different Graphene Layers to Enhance or Prevent Corrosion of Polycrystalline Copper. *RSC Adv.* **2018**, *8* (27), 15181–15187.
(40) Xu, X.; Yi, D.; Wang, Z.; Yu, J.; Zhang, Z.; Qiao, R.; Sun, Z.; Hu, Z.; Gao, P.; Peng, H.; et al. Greatly Enhanced Anticorrosion of Cu by Commensurate Graphene Coating. *Adv. Mater.* **2018**, *30* (6).
(41) Gao, L.; Guest, J. R.; Guisinger, N. P. Epitaxial Graphene on Cu(111). *Nano Lett.* **2010**, *10* (9), 3512–3516.
(42) Rasool, H. I.; Song, E. B.; Allen, M. J.; Wassei, J. K.; Kaner, R. B.; Wang, K. L.; Weiller, B. H.; Gimzewski, J. K. Continuity of Graphene on Polycrystalline Copper. *Nano Lett.* **2011**, *11* (1), 251–256.
(43) Zhang, Y.; Gao, T.; Gao, Y.; Xie, S.; Ji, Q.; Yan, K.; Peng, H.; Liu, Z. Defect-like Structures of Graphene on Copper Foils for Strain Relief Investigated by High-Resolution Scanning Tunneling Microscopy. *ACS Nano* **2011**, *5* (5), 4014–4022.
(44) Walter, A. L.; Nie, S.; Bostwick, A.; Kim, K. S.; Moreschini, L.; Chang, Y. J.; Innocenti, D.; Horn, K.; McCarty, K. F.; Rotenberg, E. Electronic Structure of Graphene on Single-Crystal Copper Substrates. *Phys. Rev. B - Condens. Matter Mater. Phys.* **2011**, *84* (19), 1–7.
(45) Braeuninger-Weimer, P.; Brennan, B.; Pollard, A. J.; Hofmann, S. Understanding and Controlling Cu Catalyzed Graphene Nucleation: The Role of Impurities, Roughness and Oxygen Scavenging. *Chem. Mater.* **2016**, *28* (24), 8905–8915.
(46) Duong, D. L.; Han, G. H.; Lee, S. M.; Gunes, F.; Kim, E. S.; Kim, S. T.; Kim, H.; Ta, Q. H.; So, K. P.; Yoon, S. J.; et al. Probing Graphene Grain Boundaries with Optical Microscopy. *Nature* **2012**, *490* (7419), 235–239.
(47) Jia, C.; Jiang, J.; Gan, L.; Guo, X. Direct Optical Characterization of Graphene Growth and Domains on Growth Substrates. *Sci. Rep.* **2012**, *2*, 707.
(48) Qi, Z.; Zhu, X.; Jin, H.; Zhang, T.; Kong, X.; Ruoff, R. S.; Qiao, Z.; Ji, H. Rapid Identification of the Layer Number of Large-Area Graphene on Copper. *Chem. Mater.* **2018**, *30* (6), 2067--2073.
(49) Ly, Thuc Hue and Duong, Dinh Loc and Ta, Quang Huy and Yao, Fei and Vu, Quoc An and Jeong, Hye Yun and Chae, Sang Hoon and Lee, Y. H. Nondestructive Characterization of Graphene Defects. *Adv. Funct. Mater.* **2013**, *23* (41), 5183--5189.
(50) Constable, F. H. The Cause of the Colours Shown during the Oxidation of Metallic Copper. *Proc. Roy. Soc* **1927**, *117*, 376–386.
(51) McAdam, D. J.; Geil, G. W. Rate of Oxidation of Typical Nonferrous Metals as Determined by Interference Colors of Oxide Films. *J. Res. Natl. Bur. Stand. (1934).* **1942**, *28* (5), 593.
(52) Gwathmey, A. T.; Benton, A. F. The Reaction of Gases on the Surface of a Single Crystal of Copper. I: Oxygen. *J. Phys. Chem.* **1942**, *46* (8), 969–980.
(53) Miley, H. A. Copper Oxide Films. *J. Am. Chem. Soc.* **1937**, *59* (3), 2626–2629.
(54) Young, K. T.; Phillips, S. S.; Coley, J. T. T.; Perini, C. J.; Hitchcock, D. A.; Serkiz, S. M.; Vogel, E. M. The Impact of Defect Density, Grain Size, and Cu Orientation on Thermal Oxidation of

Graphene-Coated Cu. *Appl. Surf. Sci.* **2019**, *478*, 959–968.
(55) Lee, U.; Han, Y.; Lee, S.; Suk, J.; Lee, Y. H.; Kim, U. J.; Son, H. Time Evolutional Studies on Strain and Doping of Graphene Grown on a Copper Substrate Using Raman Spectroscopy. *ACS Nano* **2019**, *14* (1), 919–926.
(56) Scardamaglia, M.; Struzzi, C.; Zakharov, A.; Reckinger, N.; Zeller, P.; Amati, M.; Gregoratti, L. Highlighting the Dynamics of Graphene Protection toward the Oxidation of Copper Under Operando Conditions. *ACS Appl. Mater. Interfaces* **2019**, *11* (32), 29448–29457.
(57) Biesinger, M. C. Advanced Analysis of Copper X-Ray Photoelectron Spectra. *Surf. Interface Anal.* **2017**, *49* (13), 1325–1334.
(58) Moulder, J.; Stickle, W.; Sobol, P. E.; Bomben, D. K. *Handbook of X-Ray Photoelectron Spectroscopy*; Perkin-Elmer, 1992.
(59) Platzman, I.; Brener, R.; Haick, H.; Tannenbaum, R. Oxidation of Polycrystalline Copper Thin Films at Ambient Conditions. *J. Phys. Chem. C* **2008**, *112* (4), 1101–1108.
(60) Lee, S. Y.; Mettlach, N.; Nguyen, N.; Sun, Y. M.; White, J. M. Copper Oxide Reduction through Vacuum Annealing. *Appl. Surf. Sci.* **2003**, *206* (1), 102–109.
(61) Weatherup, R. S.; Eren, B.; Hao, Y.; Bluhm, H.; Salmeron, M. B. Graphene Membranes for Atmospheric Pressure Photoelectron Spectroscopy. *J. Phys. Chem. Lett.* **2016**, *7* (9), 1622–1627.
(62) Mohiuddin, T. M. G.; Lombardo, A.; Nair, R. R.; Bonetti, A.; Savini, G.; Jalil, R.; Bonini, N.; Basko, D. M.; Galiotis, C.; Marzari, N.; et al. Uniaxial Strain in Graphene by Raman Spectroscopy: G Peak Splitting, Grüneisen Parameters, and Sample Orientation. *Phys. Rev. B - Condens. Matter Mater. Phys.* **2009**, *79* (20), 1–8.
(63) Lee, J. E.; Ahn, G.; Shim, J.; Lee, Y. S.; Ryu, S. Optical Separation of Mechanical Strain from Charge Doping in Graphene. *Nat. Commun.* **2012**, *3* (May), 1024–1028.
(64) Neumann, C.; Reichardt, S.; Venezuela, P.; Drögeler, M.; Banszerus, L.; Schmitz, M.; Watanabe, K.; Taniguchi, T.; Mauri, F.; Beschoten, B.; et al. Raman Spectroscopy as Probe of Nanometre-Scale Strain Variations in Graphene. *Nat. Commun.* **2015**, *6* (8429), 1–7.
(65) Braeuninger-weimer, P.; Burton, O.; Weatherup, R. S.; Wang, R.; Dudin, P.; Brennan, B.; Pollard, A. J.; Bayer, B. C.; Veigang-radulescu, V. P.; Meyer, J. C.; et al. Reactive Intercalation and Oxidation at the Buried Graphene-Germanium Interface. *APL Mater.* **2019**, *7* (7), 071107.
(66) Luo, B.; Whelan, P. R.; Shivayogimath, A.; Mackenzie, D. M. A.; Boggild, P.; Booth, T. J. Copper Oxidation Through Nucleation Sites of Chemical Vapor Deposited Graphene. *Chem. Mater.* **2016**, *28* (11), 3789–3795.
(67) Wu, R.; Gan, L.; Ou, X.; Zhang, Q.; Luo, Z. Detaching Graphene from Copper Substrate by Oxidation-Assisted Water Intercalation. *Carbon* **2016**, *98* (13382), 138–143.
(68) Li, D. Y.; Li, W. Electron Work Function: A Parameter Sensitive to the Adhesion Behavior of Crystallographic Surfaces. *Appl. Phys. Lett.* **2001**, *79* (26), 4337–4338.
(69) Haas, G. A.; Thomas, R. E. Work Function and Secondary Emission Studies of Various Cu Crystal Faces. *J. Appl. Phys.* **1977**, *48* (1), 86–93.
(70) Godowski, P. J.; Onsgaard, J. Work Function of Vicinal Copper Surfaces. *Acta Phys. Pol. A* **2013**, *123* (1), 115–117.
(71) Derry, G. N.; Kern, M. E.; Worth, E. H. Recommended Values of Clean Metal Surface Work Functions. *J. Vac. Sci. Technol. A Vacuum, Surfaces, Film.* **2015**, *33* (6), 060801.
(72) Smoluchowski, R. Anisotropy of the Electronic Workfunction of Metals. *Phys. Rev.* **1941**, *60* (9), 661–674.
(73) Wang, J.; Wang, S. Surface Science Surface Energy and Work Function of Fcc and Bcc Crystals : Density Functional Study. *Surf. Sci.* **2014**, *630*, 216–224.
(74) Liang, S. J.; Ang, L. K. Electron Thermionic Emission from Graphene and a Thermionic Energy Converter. *Phys. Rev. Appl.* **2015**, *3* (1), 1–8.
(75) Xu, K.; Zeng, C.; Zhang, Q.; Yan, R.; Ye, P.; Wang, K.; Seabaugh, A. C.; Xing, H. G.; Suehle, J. S.; Richter, C. A.; et al. Direct Measurement of Dirac Point Energy at the Graphene/Oxide

Interface. *Nano Lett.* **2013**, *13* (1), 131–136.
(76) Christodoulou, C.; Giannakopoulos, A.; Nardi, M. V.; Ligorio, G.; Oehzelt, M.; Chen, L.; Pasquali, L.; Timpel, M.; Giglia, A.; Nannarone, S.; et al. Tuning the Work Function of Graphene-on-Quartz with a High Weight Molecular Acceptor. *J. Phys. Chem. C* **2014**, *118* (9), 4784–4790.
(77) Li, W.; Li, D. Y.; Li, W. On the Correlation between Surface Roughness and Work Function in Copper On the Correlation between Surface Roughness and Work Function in Copper. *J. Chem. Phys.* **2005**, *122* (064708), 1–6.
(78) Vol, S.; Periodicals, W. An Experimental Viewpoint on the Information Depth of EBSD. *Scanning* **2016**, *38* (2), 164–171.
(79) Kraus, J.; Böcklein, S.; Reichelt, R.; Günther, S.; Santos, B.; Menteş, T. O.; Locatelli, A. Towards the Perfect Graphene Membrane? – Improvement and Limits during Formation of High Quality Graphene Grown on Cu-Foils. *Carbon* **2013**, *64*, 377–390.
(80) Galbiati, M.; Stoot, A. C.; Mackenzie, D. M. A.; Bøggild, P.; Camilli, L. Real-Time Oxide Evolution of Copper Protected by Graphene and Boron Nitride Barriers. *Sci. Rep.* **2017**, *7*, 39770.
(81) Camilli, L.; Cassidy, A.; Hornekær, L.; Bøggild, P. Challenges for Continuous Graphene as a Corrosion Barrier. *2D Mater.* **2019**, *6* (2), 022002.
(82) Shen, L.; Zhao, Y.; Wanf, Y.; Song, R.; Yao, Q.; Chen, S.; Chai, Y. Long-Term Corrosion Barrier with Insulating Boron Nitride Monolayer. *J. Mater. Chem. A* **2016**, *4*, 5044–5050.
(83) Bunch, J. S.; Verbridge, S. S.; Alden, J. S.; Zande, A. M. Van Der; Parpia, J. M.; Craighead, H. G.; Mceuen, P. L. Impermeable Atomic Membranes from Graphene Sheets. *Nano Lett.* **2008**, *8* (8), 2458–2462.
(84) Leenaerts, O.; Partoens, B.; Peeters, F. M. Graphene: A Perfect Nanoballoon. *Appl. Phys. Lett.* **2008**, *93* (19), 10–13.
(85) Cancado, L. G.; Jorio, A.; Ferreira, E. H. M.; Stavale, F.; Achete, C. A.; Capaz, R. B.; Moutinho, M. V. O.; Lombardo, A.; Kulmala, T. S.; Ferrari, A. C. Quantifying Defects in Graphene via Raman Spectroscopy at Different Excitation Energies. *Nano Lett.* **2011**, *11* (8), 3190–3196.
(86) Deng, B.; Wu, J.; Zhang, S.; Qi, Y.; Zheng, L.; Yang, H.; Tang, J. Anisotropic Strain Relaxation of Graphene by Corrugation on Copper Crystal Surfaces. *Small* **2018**, *14* (22), 1800725.
(87) Kang, J. H.; Moon, J.; Kim, D. J.; Kim, Y.; Jo, I.; Jeon, C.; Lee, J.; Hong, B. H. Strain Relaxation of Graphene Layers by Cu Surface Roughening. *Nano Lett.* **2016**, *16* (10), 5993–5998.
(88) Tian, J.; Cao, H.; Wu, W.; Yu, Q.; Guisinger, N. P.; Chen, Y. P. Graphene Induced Surface Reconstruction of Cu. *Nano Lett.* **2012**, *12* (8), 3893–3899.
(89) Hattab, H.; N'Diaye, A. T.; Wall, D.; Klein, C.; Jnawali, G.; Coraux, J.; Busse, C.; Van Gastel, R.; Poelsema, B.; Michely, T.; et al. Interplay of Wrinkles, Strain, and Lattice Parameter in Graphene on Iridium. *Nano Lett.* **2012**, *12* (2), 678–682.
(90) Deng, S.; Berry, V. Wrinkled, Rippled and Crumpled Graphene: An Overview of Formation Mechanism, Electronic Properties, and Applications. *Mater. Today* **2015**, *19* (4), 197–212.
(91) Kojima, R.; Susa, M. Surface Melting of Copper with (100), (110), and (111) Orientations in Terms of Molecular Dynamics Simulation. *High Temp. - High Press.* **2002**, *34* (6), 639–648.
(92) Zhang, Y. H.; Wang, B.; Zhang, H. R.; Chen, Z. Y.; Zhang, Y. Q.; Wang, B.; Sui, Y. P.; Li, X. L.; Xie, X. M.; Yu, G. H.; et al. The Distribution of Wrinkles and Their Effects on the Oxidation Resistance of Chemical Vapor Deposition Graphene. *Carbon* **2014**, *70*, 81–86.
(93) Hakkinen, H.; Manninen, M. Computer Simulation of Disordering and Premelting of Low-Index Faces of Copper. *Phys. Rev. B* **1992**, *46* (3), 1725.
(94) Platzman, I.; Saguy, C.; Brener, R.; Tannenbaum, R.; Haick, H. Formation of Ultrasmooth and Highly Stable Copper Surfaces through Annealing and Self-Assembly of Organic Monolayers. *Langmuir* **2010**, *26* (1), 191–201.
(95) Yamamoto, S.; Bluhm, H.; Andersson, K.; Ketteler, G.; Ogasawara, H.; Salmeron, M.; Nilsson, A. In Situ X-Ray Photoelectron Spectroscopy Studies of Water on Metals and Oxides at

Ambient Conditions. *J. Phys. Condens. Matter* **2008**, *20* (18), 184025.
(96) Gattinoni, C.; Michaelides, A. Atomistic Details of Oxide Surfaces and Surface Oxidation: The Example of Copper and Its Oxides. *Surf. Sci. Rep.* **2015**, *70* (3), 424–447.
(97) Liu, T.; Chen, S.; Cheng, S.; Tian, J.; Chang, X.; Yin, Y. Corrosion Behavior of Super-Hydrophobic Surface on Copper in Seawater. *Electrochim. Acta* **2007**, *52* (28), 8003–8007.
(98) Mohamed, A. M. A.; Abdullah, A. M.; Younan, N. A. Corrosion Behavior of Superhydrophobic Surfaces: A Review. *Arab. J. Chem.* **2015**, *8* (6), 749–765.
(99) Tasić, Ž. Z.; Petrović, M. B.; Milan, M.; Milan, B. R. New Trends in Corrosion Protection of Copper. *Chem. Pap.* **2019**, *73*, 2103–2132.
(100) Lee, D.; Ahn, G.; Ryu, S. Two-Dimensional Water Diffusion at a Graphene − Silica Interface. *J. Am. Chem. Soc.* **2014**, *136*, 6634–6642.
(101) Lawton, T. J.; Pushkarev, V.; Broitman, E.; Reinicker, A.; Sykes, E. C. H.; Gellman, A. J. Initial Oxidation of Cu(Hkl) Surfaces Vicinal to Cu(111): A High-Throughput Study of Structure Sensitivity. *J. Phys. Chem. C* **2012**, *116* (30), 16054–16062.
(102) Wiame, F.; Maurice, V.; Marcus, P. Initial Stages of Oxidation of Cu(1 1 1). *Surf. Sci.* **2007**, *601* (5), 1193–1204.
(103) Armitage, A. F.; Woodruff, D. P. Initial Adsorption Kinetics of Oxygen and Sulphur on Copper Cylindrical Crystal Surfaces. *Surf. Sci.* **1982**, *114* (2–3), 414–430.
(104) Matsumoto, T.; Bennett, R. A.; Stone, P.; Yamada, T.; Domen, K.; Bowker, M. Scanning Tunneling Microscopy Studies of Oxygen Adsorption on Cu(111). *Surf. Sci.* **2001**, *471* (1–3), 225–245.
(105) Tseng, C.; Tu, K. N.; Chen, C. Comparison of Oxidation in Uni-Directionally and Randomly Oriented Cu Films for Low Temperature Cu-to-Cu Direct Bonding. *Sci. Rep.* **2018**, *8* (10671), 1–7.
(106) Jeon, B.; Sankaranarayanan, S. K. R. S. Influence of Surface Orientation and Defects on Early-Stage Oxidation and Ultrathin Oxide Growth on Pure Copper. *Philos. Mag.* **2011**, *91* (32), 4073--4088.
(107) Keil, P.; Lutzenkirche-Hecht, D.; Frahiri, R. Investigation of Room Temperature Oxidation of Cu in Air by Yoneda-XAFS. *AIP Conf. Proc.* **2007**, *882* (1), 490–492.
(108) Zhang, H.; Ren, S.; Pu, J.; Xue, Q. Barrier Mechanism of Multilayers Graphene Coated Copper against Atomic Oxygen Irradiation. *Appl. Surf. Sci.* **2018**, *444*, 28–35.
(109) Wu, M.; Zhang, Z.; Xu, X.; Zhang, Z.; Duan, Y.; Dong, J.; Qiao, R.; You, S.; Wang, L.; Qi, J.; et al. Seeded Growth of Large Single-Crystal Copper Foils with High-Index Facets. *Nature* **2020**, *581* (7809), 406–410.
(110) Huang, P. Y.; Ruiz-Vargas, C. S.; van der Zande, A. M.; Whitney, W. S.; Levendorf, M. P.; Kevek, J. W.; Garg, S.; Alden, J. S.; Hustedt, C. J.; Zhu, Y.; et al. Grains and Grain Boundaries in Single-Layer Graphene Atomic Patchwork Quilts. *Nature* **2011**, *469* (7330), 389–392.
(111) Fauzi, F. B.; Ismail, E.; Ani, M. H.; Syed Abu Bakar, S. N.; Mohamed, M. A.; Majlis, B. Y.; Md Din, M. F.; Azam Mohd Abid, M. A. A Critical Review of the Effects of Fluid Dynamics on Graphene Growth in Atmospheric Pressure Chemical Vapor Deposition. *J. Mater. Res.* **2018**, *33* (9), 1088–1108.
(112) Wood, J. D.; Schmucker, S. W.; Lyons, A. S.; Pop, E.; Lyding, J. W. Effects of Polycrystalline Cu Substrate on Graphene Growth by Chemical Vapor Deposition. *Nano Lett.* **2011**, *11* (11), 4547–4554.
(113) Gregoratti, L.; Al-Hada, M.; Amati, M.; Brescia, R.; Roccella, D.; Sezen, H.; Zeller, P. Spatially Resolved Photoelectron Spectroscopy from Ultra-High Vacuum to Near Ambient Pressure Sample Environments. *Top. Catal.* **2018**, *61* (12–13), 1274--1282.
(114) Gregoratti, L.; Barinov, A.; Benfatto, E.; Cautero, G.; Fava, C.; Lacovig, P.; Lonza, D.; Kiskinova, M.; Tommasini, R.; Mähl, S.; et al. 48-Channel Electron Detector for Photoemission Spectroscopy and Microscopy. *Rev. Sci. Instrum.* **2004**, *75* (1), 64–68.

Table of Contents Graphic: